Acta Materialia **49**, 3409–3420 (2001) / doi: 10.1016/S1359-6454(01)00256-7

Investigation of metal foam formation by microscopy and ultra small-angle neutron scattering

John Banhart
Fraunhofer-Institute for Advanced Materials
Wiener Str. 12, 28359 Bremen, Germany

Dieter Bellmann, Helmut Clemens
Institute for Materials Research, GKSS Research Centre
Max-Planck Str., 21502 Geesthacht, Germany

Abstract

Zinc foams were prepared by applying the powder compaction method which comprises mixing zinc powder with a small fraction of a blowing agent, compacting this mix and creating a foam by heat treatment above the melting temperature of the metal. The foaming process which normally leads to a volume expansion of some 500% was artificially stopped in very early stages by quenching. The resulting samples with porosities below 20% were then characterised by microscopy and ultra small-angle neutron scattering (USANS). Foam microstructures, pore morphologies, the locations of the blowing agent particles, pore and particle size distributions and total pore volume fractions were determined. Two mechanisms for pore formation could be identified by microscopy. The pore growth behaviour for different size regimes could be obtained from the USANS distribution curves, thus giving insight into the early stages of metal foam formation.

Zusammenfassung

Zinkschäume wurden aus Pulverpreßlingen hergestellt. Hierzu wurden Mischungen aus Zinkpulver und einem kleinen Anteil eines Treibmittels angesetzt, verdichtet und anschließend durch Wärmebehandlung oberhalb des Schmelzpunktes des Metalls geschäumt. Der Schäumprozeß, der normalerweise zu einer Volumenexpansion von 500% oder mehr führt, wurde durch Abschrecken unterbrochen, was zu Porositäten unter 20% führte. Die Proben wurden mittels Licht- und Elektronenmikroskopie sowie Neutronenkleinwinkelstreuung untersucht und Schaummikrostrukturen, Porenmorphologien, der Ort der Treibmittelteilchen sowie Poren- bzw. Partikelgrößen-Verteilungsfunktionen ermittelt. Es konnten zwei Porenbildungsmechanismen identifiziert und der Ablauf des Blasenwachstums charakterisiert werden. Die gemessenen Daten erlauben eine Aussage über das frühe Schäumstadium in Metallen.

Keywords: ultra small-angle neutron scattering, powder processing, zinc, foam

1 Introduction

There has been renewed interest in cellular metals in the past few years [1][2]. Among the different types of materials which are available, metallic foams are especially attractive because they are fairly inexpensive and have attractive mechanical properties. By foaming one usually means releasing gas in a liquid, ensuring that the gas bubbles do not escape, and finally stabilising the liquid foam by cooling [3]. A manufacturing method for producing closed-cell metal foams from metal powders was developed some years ago [4][5][6]. The process consists of mixing metal powder and a powdered blowing agent and compacting the mix into a dense semi-finished product (called *foamable precursor material*) by hot pressing, extrusion, powder rolling or other methods. In a final step the foamable precursor material is expanded by heating to above its melting point. This transfers the metal into a semi-liquid viscous state and simultaneously makes the blowing agent decompose, thus releasing gas and creating a highly porous structure. Up to now the main interest has been on aluminium and aluminium alloy foams, although a number of other metals and alloys such as zinc, lead, tin, steels, and gold can also be foamed. For each alloy a suitable blowing agent has to be found. The melting point of the alloy and the decomposition range of the blowing agent have to be co-ordinated to allow the formation of metal foam. Titanium hydride and zirconium hydride which set free hydrogen at temperatures above 380°C-400°C are suitable agents for zinc- and aluminium-based alloys because they release large gas volumes and have a wide decomposition interval.

Although metal foaming technology is quite advanced now - large size automotive components can be manufactured [7] – , the properties of metal foams and the physics of metal foam generation and evolution are just starting to be explored. Various characterisation methods can be applied as summarised in **Table 1**. Quite some work on the structural characterisation of metal foams has been carried out. Generally, fully expanded metal foams are investigated. One objective is to establish relationships between structure and properties. For example, optical microscopy and image analysis have been used to characterise pore size and shape distributions in a given cutting plane through a sample [8]. Methods of quantitative stereology have to be used to extract a true picture of the foam from the data obtained in this way. However, statistics may be insufficient and an unfortunate choice of the cutting plane can lead to a misleading picture of the foam structure. To avoid this problem computed X-ray tomography has been applied [9][10][11]. In this way, non-destructive three-dimensional sampling of the entire foam becomes possible.

In order to understand how the foam structure is generated it is useful to investigate not only fully expanded foams, but also foams in the early stages of evolution. For this one can apply either in-situ or ex-situ methods. In the former case the evolving foam is monitored during its expansion, e.g. by recording a time-dependent expansion curve [12], or even by generating a picture of the evolving foam using X-ray radioscopic methods [13][14]. In contrast, an ensemble of samples in which each sample represents one particular stage of evolution of the foam is analysed in ex-situ investigations, e.g. by microscopy [12]. The individual samples are prepared by interrupting the foaming process at a given time.

If one wants to study the very early stages of foaming, i.e., stages in which the pores are just being formed, one has to apply methods with act on the appropriate length scale which ranges from some tens of nanometers to several micrometers. Optical or electron microscopy, for example, are suitable for investigations if two-dimensional information is sufficient. Often, however, one is less interested in mapping individual pores, but wants to obtain a three-dimensional average of a pore size distribution. Such distributions can be useful, for example, as input data for model calculations of the foam generation process [15]. Ultra small-angle neutron scattering (USANS) is a promising method for obtaining this information because scattering of cold neutrons at very small wave vectors provides exactly the size range required. USANS was therefore chosen for the present study. However, it is well-known that the analysis of data obtained from USANS is highly non-trivial and can only be performed successfully if one is able to provide supplementary information on the kind and shape of the scattering centres invoked [16][17]. Therefore we carried out in parallel both microscopic studies and USANS measurements to establish and assess the usefulness of the approach. In order to encounter a fairly simple situation in this study, zinc foams were chosen because zinc is known to show a very simple bubble formation pattern when foamed with zirconium hydride, i.e., the bubbles generated are always almost spherical even in the very early stages of foam formation, whereas pore formation in aluminium alloys, for example, is much more complicated [3][12].

2 Experimental

2.1 Sample preparation

Zinc foam samples were prepared in a three-stage process comprising powder mixing, hot pressing and foaming. First, zinc powder (Eckart-Dorn, type AS; <0.045 mm) was mixed with 0.3 wt.% (corresponding to 0.39 vol.%) of zirconium hydride (ZrH_2) powder (Chempur, 99.7% purity) which acted as a blowing agent. For reference measurements, the blowing agent was omitted for one sample, i.e., zinc powders were also processed with no additive. In a second step the powder mix (or the pure metal powder) was filled into a cylindrical die with 32 mm diameter and was pressed at a temperature of 350 °C and a pressure of 110 MPa for 30 minutes. 50 g of powder was used for each sample. The resulting cylindrical tablets were cut into 4 mm thick slices by electric discharge machining (EDM). For foaming a furnace was pre-heated to 440°C. The furnace was equipped with a flat sample substrate onto which a thermocouple was attached. The temperature of the sample support was found to be nearly constant even after the furnace door was opened for a short time in order to place the cold (but very light) sample on it. The sample was quickly warmed up by the pre-heated substrate where it remained for a given foaming time t, after which it was removed and immediately quenched to room temperature with pressurised air.

A 0.4 mm thick slice was cut out from the centre of the solidified foamed sample by EDM for the USANS measurements. The remaining two outer slices were used for microscopy. The densities of the thin slices were determined by buoyancy measurement. Table 2 lists all samples examined in the study, including a sample without blowing agent, an unfoamed specimen with blowing agent and 8 different foamed samples. The unfoamed specimens contained about 1% residual porosity. Foaming led to a slight increase in porosity up to 2.6% after 110 s, thereafter a rapid volume increase was recorded in the following 10 seconds of exposure to heat. As the onset of foaming was so abrupt, it was difficult to cover the range of rapid expansion equally with samples using the available equipment. Thus we had to prepare a larger number of foams to obtain the two samples fitting into the range.

In order to obtain information about the temperature course in the foaming metals, some reference samples were foamed with a thermocouple directly attached. For this an inconel-encased Ni-CrNi thermocouple was inserted into a small orifice in the upper wall of the furnace from where it was led to the sample in a straight line. By pushing the thermocouple downwards the sample could be contacted perpendicular to its surface. The thermocouple was stiff enough to bear a load of approximately 2 N. This ensured a good

contact at all times. **Figure 1** shows the result of one such measurement. The thermocouple was at 440°C in the pre-heated furnace before the cold precursor material was placed onto the substrate and the thermocouple was brought into contact with it. Closing the furnace lid 3 seconds later defines the zero of time (t=0). The temperature drops immediately until it meets the rising temperature of the heated sample. As the melting point of the metal is reached, the thermocouple starts to penetrate the softening material. This penetration can be detected quite easily and is marked in the plot. For the production of samples, the foams were removed and quenched after certain times t as listed in Table 2 and marked in **Figure 1**. For pure temperature measurements, however, the samples were not removed. One finds that the sample temperature remains at about 420°C until all the material has melted, after that it climbs to the furnace temperature of 440°C (not shown).

The inset shows a magnification of the melting range. The experimentally determined softening temperature indicates that melting occurs about 1°C below the known melting point of Zn (419°C). This could be a consequence of impurities in the metal which may lead to earlier melting or just an offset in the temperature measurement. After melting a slight dip in the temperature curve occurs. Similar features were also observed in other measurements. They reflect interference effects between the higher furnace temperature and the temperature changes in the sample which are governed by the heat consumption by the melting metal in the temperature range under discussion.

2.2 Powder properties

The particle size distribution of all powders were measured using a Coulter LS130 laser particle size analyser in which the powders are dispersed in a liquid, after which Fraunhofer diffraction of laser light from the particles is measured. Particle volume distributions and average particle sizes were determined in this way. The average size for zinc powder particles was 29 μm, whereas the ZrH_2 blowing agent powder particles were on average 14.7 μm in size. The particle size distribution will be used in the discussion in Sec. 3.2.

2.3 Ultra small-angle neutron scattering (USANS)

2.3.1 Experimental set-up

The principal set-up used for USANS studies is shown in **Figure 2**. A part of the neutron beam coming from the cold source of the reactor is reflected by a pre-monochromator (perfect silicon Si(111) crystal, Bragg-angle 45°) into the double crystal diffractometer (DCD) and then monochromatised using a multi-reflection mirror (quintuple-bounce channel-cut perfect Si(111) crystal with cadmium inserts) [18][19]. After passing a holding device for changing samples the angle distribution of the neutrons is measured by rotating an analyser crystal (smallest angle steps of 10^{-5} degree) which is identical to the monochromator crystal. The neutrons have a wavelength of λ = 0.443 nm and a wavelength dispersion of $\Delta\lambda/\lambda \approx 10^{-3}$%. The average flux at the sample position is about 500 cm^{-2} s^{-1}. The rocking curve (RC) (the angle distribution of the neutrons without a sample in the beam) is given by the convolution of the reflectivity curves of the two perfect crystals. With a sample between the two crystals, the RC curve includes scattering from the sample. The accessible scattering range is 10^{-5} - 10^{-1} nm^{-1}. Using this technique inhomogeneities (particles, pores, etc.) from 24 μm down to 0.03 μm in size are detectable.

2.3.2 Scattering in heterogeneous samples [16]

For elastic neutron scattering, the scattering vector **q** is defined by the difference of the wave vectors before and after scattering. The absolute value is given by

$$|\mathbf{q}| \equiv q = \frac{4 \cdot \pi}{\lambda} \sin\frac{\theta}{2}, \qquad (1)$$

where λ is the neutron wavelength and θ the scattering angle.

The macroscopic scattering cross section Σ for neutrons incident on a sample consisting of N nuclei in a volume V with a nuclear density n = N/V is given by

$$\Sigma = n\,\sigma_{coh}, \qquad (2)$$

where $\sigma_{coh} = 4\,\pi\,b^2$ represents the microscopic coherent scattering cross section, and b is the bound coherent scattering length, a nuclear property [20]. The transmission T due to scattering is given by $T = e^{-\Sigma \cdot D}$, D being the sample thickness.

A two-phase model has been used to analyse the scattering curves (contributions from interparticle interference are neglected): A binary system of N_p identical particles with the scattering length density $\eta_p = b_p/v_p$ has been considered, embedded in a matrix of homogenous scattering length density $\eta_m = b_m/v_m$, where b_p is the scattering length averaged

over the particle volume and v_p is the atomic volume in the particle. b_m and v_m are the corresponding values for the matrix. The scattering length density difference $\Delta\eta$ of the matrix and particles is given by:

$$\Delta\eta = (\eta_m - \eta_p)\,. \tag{3}$$

Using the single-particle form factor $F_p(\mathbf{q})$,where $\left|F_p(0)\right|^2 = 1$, and denoting the solid angle Ω and the particle volume V_p, the differential macroscopic scattering cross section is:

$$\frac{d\Sigma}{d\Omega}(\mathbf{q}) = V_p^2 \cdot N_p \cdot (\Delta\eta)^2 \cdot \left|F_p(\mathbf{q})\right|^2 . \tag{4}$$

This scattering law has to be generalised for the scattering from a random system of non-identical particles without orientational correlations.

The total apparent scattering probability z (scattering power)

$$z = \Sigma \cdot D = D \cdot \int \frac{d\Sigma}{d\Omega}(q)d\Omega\,. \tag{5}$$

results for spheres of radius R in the equation

$$z = \Sigma \cdot D = \frac{3}{2} \cdot D \cdot R \cdot \lambda^{2\cdot} f \cdot (\Delta\eta)^2 . \tag{6}$$

The scattering power is proportional to the product of the total volume fraction and the square of the scattering length density difference. Therefore the shape of the size distribution is not influenced by the value of η chosen, as only the total volume fraction f changes.

It is well known that for $z > 0.1$ the influence of multiple scattering can no longer be neglected. Thus, the only way to decrease multiple scattering for a given material and wavelength is to reduce the sample thickness D. As this is often not feasible with real samples, one tries to reduce D by numerical algorithms.

As the scattering length of ZrH_2 (determined from the scattering lengths of Zr and H which are $0.716\cdot10^{-12}$ cm and $-0.3739\cdot10^{-12}$ cm, respectively) is only b = $-0.0106\cdot10^{-12}$ cm and the blowing agent content is quite small (0.3 wt.%) the influence of ZrH_2 is neglected. This means that features in the scattering curve which are not resolved explicitly by the fit procedure have to be attributed to zirconium hydride. The scattering length of zinc is $0.568\cdot 10^{-12}$ cm, which corresponds to a scattering length density difference between Zn and pores (η_{pores}=0) of $\Delta\eta = 3.73\cdot10^{10}$ cm^{-2} , assuming a mean metal density of 7.13 g cm^{-3} .

The largest heterogeneities, which can be detected with a double crystal diffractometer (DCD), are limited by the so called Darwin width, which is a result of dynamical diffraction theory [21][22]. This value determines the resolution of DCD. For a perfect silicon Si(111) crystal the Darwin width in the symmetrical Bragg case is given by

$$\Delta\theta = \frac{b_c \cdot e^{-W} \cdot |F| \cdot N \cdot \lambda^2}{4\pi \cdot \sin 2\theta_B}, \tag{7}$$

where the following quantities have been used: number density of Si particles N =4.99·10^{22} cm^{-3}, geometrical structure factor $|F| = 4 \cdot \sqrt{2}$, coherent scattering length b_c = 0.41491·10^{-12} cm, Debye-Waller factor $e^{-W} \cong 1$, neutron wavelength λ=0.443 nm, Bragg angle θ_B =45°.

This yields a Darwin width (full width of the rocking curve) of $\Delta\theta$ =18.3 μrad. The upper limit of particle sizes is determined by the half width of this Darwin width:

$$q_{\min} = \frac{2\pi}{\lambda} \cdot \Delta\theta / 2 = 1.3 \cdot 10^{-4}\, nm^{-1}. \tag{8}$$

Measurements will not allow one to resolve structural details in real space over distances greater than d_{max} and smaller than d_{min}:

$$d_{\max} \cong \frac{\pi}{q_{\min}} \cong 24\mu m, \quad d_{\min} \cong \frac{\pi}{q_{\max}} \cong 30nm, \tag{9}$$

where $q_{max} \approx 0.1$ nm^{-1} is the maximum value accessible in the experiment.

2.3.3 Analysis of USANS data

The distribution of pores and other scattering centres, such as blowing agent or unwanted impurities in the metallic matrix was determined from the measured scattering curves using a simplified model. The underlying assumptions of this model were: (i) pores and impurities have sharp boundaries and (ii) pores and impurities are spherical in shape. In principle the relation between scattering curve and size distribution of pores or impurities is one-to-one within this model, but practical limitations introduce some ambiguities, namely the statistical error of the single $I(q_i)$ measurement and the limitation of the q range. For this a numerical fit procedure was applied. A trial distribution function of scattering objects was modified until the resulting model scattering curve $I_{th}(q)$ approximated the experimental curve $I_{exp}(q)$ as much as possible, i.e. the quantity

$$\chi^2 = \frac{1}{M} \sum_{i=1}^{M} \frac{(I_{\exp}(q_i) - I_{th}(q_i))^2}{\sigma_i^2} \tag{10}$$

was minimised. Here M is the number of q-points used for the measurements and σ_i is the mean square deviation of the i-th measurement. The indirect Fourier transformation method applied allowed for an approximation of the experimental scattering curve by choosing a log-normal function as pore size distribution [23]. The routines used for the analysis of the scattering curves only allow one to distinguish between two phases, therefore multi-phase scattering centres in a homogeneous matrix cannot be accounted for at the moment. In the case of the metal foams investigated in this work we have a system which contains at least three phases, namely the nearly homogeneous zinc matrix, the pores and the blowing agent (ZrH_2), which gradually decomposes to Zr and H_2. The real situation has to be simplified in order to be described by the model.

Because the ZrH_2 scattering length is close to that of pores, the blowing agent will yield a nearly identical scattering contribution. Thus, in many cases these contributions are indistinguishable. Therefore, we shall speak of *scattering centres*, when discussing either pores or blowing agent particles.

Some measured scattering data (i.e. the relative intensity versus scattering vector) for various zinc samples are shown in **Figure 3**. Also displayed are the calculated scattering curves which have been derived by analysis based on the particle size distributions to be discussed later in Sec. 3.2. These curves agree well with the measured data. The integrated intensity of all curves is nearly equal, only reduced by neutron absorption and incoherent scattering. The effect the samples is to scatter neutrons from the rocking curve into the range of larger scattering vectors. Therefore the intensity decreases at $q \approx 0$ with increasing size of pores, and the half-width of the scattering curves is widened. For samples containing blowing agent the scattering probability is high and because of the large size of scattering centres quite some multiple scattering occurs.

The differential macroscopic cross section shown in **Figure 4** describing the scattering probability increases from Zn without blowing agent to the Zn sample foamed for 120 s. Here the cross sections of the Zn samples with foaming times from 60 s to 110 s lie in a relatively narrow band. A pronounced effect of foaming only occurs for foaming times beyond 110 s.

3 Results and Discussion

3.1 Microscopy

All the unfoamed and foamed samples were characterised by light microscopy and

scanning electron microscopy (SEM). For light microscopy samples were embedded in black resin and polished. **Figure 5a-b** shows both the unfoamed precursor containing 0.3 wt.% ZrH_2 and the sample foamed for 120 s. The samples were not etched. The image of the precursor reveals that the blowing agent particles are uniformly distributed in the homogeneous metallic (Zn) matrix. No porosity is visible at the low magnification used. Foaming then leads to the formation of pores. As microscopic pores can be best investigated using electron microscopy, only the most expanded sample is shown. Quite clearly, a large number of pores have been created after 120 s of heating, their spatial distribution being quite uniform. The pores size varies considerably, the largest visible pores having about 140 μm diameter. After 110 s (image not shown), the pores are much smaller. Therefore, massive pore inflation starts in the time interval between 110 and 120 s.

Electron microscopy reveals more details of the emerging foam as demonstrated in the various images displayed in **Figure 6a-e**. In order to make the grain boundaries more visible and to open micro-pores which might have been smeared out after polishing, the samples were etched in 2% alcoholic HNO_3 solution for 1 minute. The unfoamed sample not containing any blowing agent (**Figure 6a**) exhibits a uniform and practically pore-free microstructure. The few pores visible (which account for the residual porosity already detected in the density measurements) are mostly about 2-3 μm in diameter. The grain boundaries are clearly visible. Features associated with such grains occur on a length scale of 5 to 40 μm which is compatible with the measured powder size spectrum.

Unfoamed samples which contain 0.3 wt.% ZrH_2 have a similar microstructure. The grain structure is again on a scale of up to some tens of micrometers. Looking at the sample at a slightly higher magnification (**Figure 6b**) some additional features become evident. As to be expected, the blowing agent particles are well visible. Energy-dispersive X-ray analysis was used to distinguish such particles from impurities that occasionally occur in the precursor such as SiO_2, Fe and Cr, for example. The ZrH_2 particle shown in **Figure 6b** is about 8 μm in diameter and is therefore slightly below the average size. What is typical is the irregular shape and also the gap between the hydride and the metallic matrix, indicating that there is no bonding between hydride and metal. Furthermore, the inset shows a region which is enlarged by a factor of about 3. A cluster of small micro-pores can be identified with sizes ranging from 0.2 to 0.4 μm. Such clusters appear quite frequently in the sample.

A foamed sample is displayed in **Figure 6c** and **6d**. Two regions are shown of this sample foamed for 110 s. The first exhibits a ZrH_2 particle, size about 5×7 μm, which is

surrounded by an annular void. Apparently the gas released by the blowing agent particle has lead to local pore formation around it. Such pores with an embedded particle are frequently found in the sample and shall be called *type-I pores*. They represent one way, in which pores can be created. Quite frequently, however, pores can be detected in which no ZrH_2 particle is visible. Some of these pores are rather shallow, others such as the one shown in **Figure 6d** are more profound. A possible explanation for the missing particle is that it has either fallen out of the shallow pores or is deeply hidden in the profound ones. However, the large number of such pores not being associated with an individual particle suggests that pores can also be created at locations well separated from a gas generating particle. Such pores, to be called *type-II pores*, mostly occur at triple grain junctions. It is therefore suspected that hydrogen gas diffuses along the grain boundaries and nucleates in the triple grain junctions thus creating a pore in this mode of non-local pore generation.

Finally, **Figure 6e** shows a large pore in the sample foamed for 120 s. The pore is about 40 μm in diameter and contains a ZrH_2 particle which has obviously inflated the pore (which is therefore of type I). The ZrH_2 particle is 8-10 μm large and therefore a typical representative of the powder size spectrum. The samples also contains type-II pores without visibly associated ZrH_2 particle (not shown).

From the microscopic images the existence of two pore types seems very probable. In order to further clarify the situation it is planned to carry out element-sensitive, non-destructive X-ray micro-tomography investigations which will allow the scanning of a selected pore and will give the information necessary to decide whether a blowing agent particle is contained in such pores or not [10].

3.2 USANS measurements

3.2.1 Unfoamed samples

The size distributions of scattering centres (differential volume fraction *v(D)* expressed in volume percent per unit size of pores and/or blowing agent particles) in unfoamed zinc samples as determined by USANS are shown in **Figure 7** for specimens with and without blowing agent.

The sample without blowing agent shows a maximum in the distribution at diameters of about 1.7 μm. Integration of the distribution curve yields a total volume fraction of scattering centres of 0.17 vol.%. The source for scattering could be residual porosity as well as other metallic impurities which are not accounted for in the data analysis. As residual porosity is certainly not spherical but more fractal in shape, the volume fraction determined

should not be thought of as a very accurate value. Indeed, the porosity determined from density measurements (0.9±0.3%) is higher. It is encouraging to see that the peak position coincides well with the observed size of many of the small pores visible in **Figure 6a**.

The specimen containing 0.3 wt.% (0.39 vol.%) ZrH_2 shows a markedly different distribution curve of scattering centres. To demonstrate this, the difference between the two curves was added to **Figure 7**. It represents the additional features introduced by the hydride powder. Two peaks in the difference distribution curve occur, one for 0.65 μm (peak I), one for 4.2 μm (peak II). There are three possible sources for small-angle scattering, namely (i) residual porosity, (ii) blowing agent particles and, (iii) other impurities which have already been mentioned (SiO_2, Fe, Cr). The blowing agent is the most obvious source for the additional scattering, but as formation of porosity could be influenced by the presence of ZrH_2 during pressing it should also be considered. As the same impurities occur in samples with and without blowing agent, these should not contribute to the difference curve. One can try to discuss the influence of pores and ZrH_2 separately. From what was said in Sec. 2.3.3 this is not possible from the USANS data because we are treating a two-phase system, where the metallic matrix is one phase. However, by making use of the measured particle size distribution of the blowing agent ZrH_2 powder (shown at the top of **Figure 7**), additional information can be obtained. ZrH_2 particles occur in significant volume fractions above particle diameters of about 2 μm. Particles with 14.7 μm diameter contribute most to the total particle volume while powder particles as large as 60 μm can still be found. As we can only resolve features with diameters up to 24 μm by USANS, the corresponding particle size spectrum is truncated in **Figure 7**. Noting that the onset of the main particle size distribution peak coincides with the division between the 2 peaks of the USANS difference curve in **Figure 7.** Therefore it seems reasonable to ascribe most of peak II to the influence of the hydride. Obviously, the powder size distribution, having its maximum at 14.7 μm, does not exactly match the USANS distribution with a maximum at 4.2 μm. This is not surprising if one keeps in mind that the particle size distribution was obtained on loose powders, whereas the USANS curve refers to ZrH_2 powder compacted into a metal matrix. Mixing and subsequent hot compaction will certainly reduce the size and morphology of the brittle hydride powder, therefore leading to a shift of the distribution maximum to lower diameters. Moreover, USANS values for diameters above 24 μm are quite uncertain due to the limitations mentioned, thus causing an artificial drop-off of the USANS distribution at large diameters. Furthermore, the observed complicated morphology of the ZrH_2 particles (see e.g. **Figure 6b**) deviates from the

assumption of spherical particles with a well defined smooth surface which might give rise to an apparent shift in particle size.

Peak I may be explained as following: As the size axis in **Figure 7** has a logarithmic scale the area under peak I looks quite large although it only accounts for about 8% of the total area under the difference curve (0.49 vol.%). The volume fraction of ZrH_2 is quite small below 1 μm particle size and there is only a very small powder fraction with diameters around 0.4 μm. This, however, is not sufficient to explain peak I. Therefore, most of this peak must arise from some porosity in the specimen in addition to the porosity already present in the sample without blowing agent. Objects of 0.7 μm diameter contribute most to peak I. The exact mechanism for the creation of this scattering contribution is not entirely clear. One can speculate that the irregularly shaped and brittle particles are not completely embedded in the metal matrix (see the area around particle shown in **Figure 6b**), thus giving rise to additional scattering from satellite voids next to the blowing agent particles. It is also possible that some gas evolution has already started during pressing of the powder mixture. Escaping hydrogen could lead to the formation of small cavities in the solid matrix. In some areas of the unfoamed sample, clusters of sub-micrometer sized pores could be found (see inset in **Figure 6b**). These are mostly 0.2 - 0.4 μm in diameter.

The total volume fraction of all scattering centres in the sample containing blowing agent as determined by USANS is 0.66%. The fraction of ZrH_2 is 0.39% and the residual porosity determined by buoyancy measurement is about 1% (±0.3%). Thus there is reasonable agreement between the USANS and conventional density measurement in this case.

3.2.2 Foamed samples

3.2.2.1 Initial foaming stage

Besides the distribution curves for unfoamed precursor material, **Figure 7** also includes the USANS distribution curve for the sample with the shortest foaming time, namely 60 seconds, i.e. for the sample which was just approaching its melting temperature and which was about to start foaming. Obviously, the effect of heat treatment is an overall reduction of the volume fraction of scattering centres in this case. The curve remains centred at about 1.5 μm but the volume fraction is reduced for all diameters. This finding corresponds with a slight increase in sample density (see Table 2) after 60 seconds of heat treatment. Possible reasons for the decrease of the volume fraction of scattering centres: (i) hydrogen losses from ZrH_2 changing the effective scattering length density of the blowing agent. This loss was

neglected in our analysis and could simulate a decrease of volume, (ii) sintering processes reducing porosity above a certain threshold temperature due to solid-state diffusion processes, (iii) impurities present in the zinc powder forming a liquid phase at temperatures below the melting point which could be absorbed by the residual porosity ("liquid-phase sintering"). As there is evidence for a real volume contraction, the first explanation can be ruled out and solid or liquid phase sintering processes must be responsible for the observed effect.

In order to find further evidence for the contraction effect - the small difference in density obtained in buoyancy measurements is not very significant - foamable zinc samples were characterised in a sintering dilatometer (Bähr TM801). Specimens with a cross section of 3x3 mm and a length of 8 mm were cut out of the hot pressed precursor material by EDM. The long axis of the samples is the direction of measurement and was chosen to be parallel to the pressing direction of the powders. Some expansion curves obtained with different heating rates are displayed in **Figure 8**. In order to extract the actual sintering effect the data were corrected for the thermal expansion of Zn using a constant expansion coefficient of $\alpha=30\cdot10^{-6}$. The corrected relative length change is fairly constant up to about 220°C after which a slight expansion starts. This expansion is followed by a sharp transition to a short phase of contraction. The onset of contraction depends on heating rate and is shifted to higher temperatures for faster heating. The linear contraction is in the order of 0.05%, i.e. the volume contraction is up to 0.15% depending on the extent of lateral expansion which was not measured. This corresponds well with the measured density change from 7.05 to 7.06 g/cm^3. However, because the heating rate during foaming (about 400K/min.) was much higher than in the dilatometer tests (about 10 K/min.) the two results are not completely equivalent. The fast heating during foaming shifts the contraction phase up to the melting point. Therefore, it seems possible that liquid phase sintering is responsible for the contraction effect.

3.2.2.2 Later foaming stages

The volume distribution curves for scattering centres in various zinc foams (as listed in Table 2**)** are shown in **Figure 9**. The entire information is displayed in the upper part of **Figure 9** in a linear plot, whereas the lower part gives insight into the range of small diameters through use of a logarithmic scale and concentrating on the samples with low porosities.

Foaming times longer than 60 s lead to an increase in volume fraction of scattering centres on almost all length scales. Obviously, for all times the distribution curves show the log-normal behaviour given by the method of the data analysis. The volume fraction drops to very low values for small diameters and it seems justified to speak of a cut-off diameter. For

large diameters the distribution curves are limited by the resolution of the method. The various curves are overlapping and the peak positions are shifted to higher diameters for longer foaming times. This shift is best illustrated in two regions of **Figure 9b** marked with arrows and numbers: region ① shows a shift of the small-particle cut-off diameter towards larger sizes for increasing foaming times. It is probable that this limit would be further shifted to the right for stages after 120 s (marked "?"). These later stages, however, are at present out of the range of the USANS technique. Region "②" displays a horizontal offset of the various distribution curves also for high volume contributions.

The inset in **Figure 9a** gives volume fractions for some fixed diameters of the scattering centres as a function of foaming time. Obviously, despite of some irregularities for small pore sizes the curves exhibit a similar pattern: for a given size the volume fraction first rises and then falls down (for 5 μm only the rise can be seen).

The physical explanation for this two-stage behaviour is straight-forward: first, small pores are created in large numbers as the sample is heated, presumably by heterogeneous nucleation. Once these pores are present, they grow steadily, driven by gas generation from the blowing agent while no new pores are developed. At the same time they also start to coalesce, thus decreasing the total number of pores and shifting the corresponding contributions of the distribution function to larger diameters. Small pores therefore eventually disappear, thus creating the cut-off diameter while large pores continue to gain importance. Foaming for 120 seconds finally leads to the growth of pores with pore diameters larger than 1 μm with the maximum of the distribution occurring at 7.5 μm diameter. As one sees from the optical micrographs, quite a significant part of the curve now lies in the regime above 24 μm, a size above which the USANS is not reliable. Therefore, it makes no sense to investigate the further foam evolution with this DCD configuration. However, by decreasing the neutron wavelength of DCD using perfect Si(311) crystals larger structures could be detectable in future experiments.

3.2.2.3 Total (integrated) volume fraction

What becomes clear at this point is that pore inflation starts rather suddenly after a longer stage of gradual expansion and proceeds very quickly. The macroscopic density shows the same behaviour (**Table 2**). From the unfoamed sample to the sample foamed up to 110 s the density decreases by just 1.5%, whereas the following 10 seconds of heat treatment result in an expansion of 17%. Similar results can be obtained from the USANS measurements by

calculating the total pore volume V'_{tot} by integration over the distribution function *v(D,t):*

$$V'_{tot}(t) = \int_0^{D_{max}} v(D,t)dD < V_{tot}(t) \ , \qquad (11)$$

The total volume fraction has been primed to emphasise that only the fraction of scattering centres accessible to USANS is included in it (D_{max} is 24 μm in our case.). **Figure 10** compares the total volume fractions determined in this way with conventionally measured relative sample densities, i.e. ρ/ρ_0, where ρ_0 is the bulk density. Obviously, the functional dependence of both quantities is very similar but the total volume fractions determined by USANS are only about half as large. The three regimes which were already discussed in the previous section are clearly visible: in region I the volume slightly decreases, in region II there is a steady volume increase which is almost linear with time as shown by the linear fit curve, whereas in region III rapid pore formation starts which eventually leads to a fully expanded foam with 85% porosity.

Possible reasons for the discrepancy between the two measurements were also addressed in the previous section: (i) deviations of pore morphology from the spherical shape and, (ii) the inability of this DCD to detect inhomogeneities greater than round about 24 μm in size. While the first explanation might apply to early foams, the second is definitely applicable to the more expanded foams, as they contain many very large pores (see **Figure 5b**).

4 Summary and outlook

Zinc foams were produced by expanding powder compacts containing zinc powder and zirconium hydride which acted as a blowing agent. By varying the time of heat treatment ("foaming time") and quenching the emerging foams after this time, different stages of early foam formation could be prepared. The combined use of image-generating light and electron microscopy and volume-averaging ultra small-angle neutron scattering allowed an insight into metal foam generation.

It has been found that by adding ZrH_2 to zinc powders the porosity of the compacted powders is increased. Either by mechanical action or by gas release during compaction porosity is created on a sub-micrometer scale. Foaming of powder compacts containing ZrH_2 first leads to a decrease of this sub-micrometer porosity resulting from either from solid-state diffusion processes or liquid-phase sintering. After this a steady creation of porosity in all size

ranges is observed. The maximum of the pore size distribution moves to larger diameters while smaller pores disappear. The foaming process is quite slow for a long period, thereafter bubble inflation starts suddenly. In this phase of accelerated bubble growth, a large pore volume is generated with a maximum pore diameter at 7.5 μm for the most mature foam investigated and many bubbles exceeding the maximum size measurable using USANS.

The SEM images of the samples used for USANS revealed many details of how pores are generated. The observed length scales are comparable with the distribution curves from USANS and some additional features can be identified. Two modes of pore creation can be distinguished: type-I pores are generated as shells around individual blowing agent particles which then growth, while type-II pores seem to be initiated at triple grain junctions and grow there without containing a blowing agent particle.

In future USANS investigations it is planned to use other hydrides beside the ZrH_2 already in use. Titanium hydride, normally used for foaming aluminium, is also suitable for foaming zinc. As other hydrides have different decomposition temperatures, this will allow additional information on the interplay between decomposition kinetics and melting of the matrix metal to be determined. Moreover, as titanium has a different neutron scattering length it will be possible to separate scattering from the pores and blowing agent particles. It could be also useful to consider compounds of Ti and Zr with deuterium instead of hydrogen. These are almost identical chemically but have very different scattering contrast to ordinary hydrides. Moreover, it could be useful to carry out complementary SANS investigations to obtain more information concerning the pore size range from 50 to 500 nm for which the USANS is not very precise, because for large scattering vectors the scattered neutron intensities are very low, nearby the background of DCD.

Future work will also include investigations of the technologically most relevant aluminium alloy foams. Such alloys, however, are expected to cause additional difficulties because pore formation is more complicated in these alloys due to the mismatch between decomposition temperature of the blowing agent and melting point of the metal. This creates crack-like pores in the solid state and makes analysis of images and USANS data more challenging.

References

[1] Banhart J., Prog. Mater. Sci., **46**(6) (in press, 2001)

[2] Banhart J., Ashby M.F., Fleck N.A., *Metal foams and porous metal structures*, (MIT-

Verlag, Bremen, 1999)

[3] Banhart J., Europhys. news **30**, 17 (1999)

[4] Baumeister J., German Patent 40 18 360 (1990), see also US Patent 5,151,246 (1992)

[5] Banhart J., Baumeister J., J. Mater. Sci. **33**, 1431 (1998)

[6] Baumgärtner F., Duarte I., Banhart J., Adv. Engnr. Mater. **2**, 168 (2000)

[7] Seeliger W., in Ref. [2], p. 29

[8] Simančík F., Jerz J., Kováčik J, Minár P., Kovové Materiály/Metallic Materials **35**, 265 (1997)

[9] Bart-Smith H., Bastawros A.-F., Mumm D.R., Evans A.G., Sypeck D.J., Wadley H.N.G., Acta Mater. **46**, 3583 (1998)

[10] Helfen L., Baumbach T., Stanzick H., Banhart J., in "*Cellular metals and metal foaming technology*", Editors: Banhart J., Ashby M.F., Fleck N.A. (MIT-Verlag, Bremen, 2001)

[11] Degischer H.P., Kottar A, in Ref. [2], p. 213

[12] Duarte I., Banhart J., Acta Mater. **48**, 2349 (2000)

[13] Banhart J., Stanzick H., Helfen L., Baumbach T., Appl. Phys. Lett. **78**, 1152 (2001)

[14] Banhart J., Stanzick H., Helfen L., Baumbach T., Advanced Engineering Materials, **3**, 407 (2001)

[15] Körner C., Singer R.F., in Ref. [2], p. 91

[16] Kostorz G., *Treatise on Materials Science and Technology*, Vol. 15: Neutron Scattering, ed: G. Kostorz, H. Herman (Academic Press, New York, 1979), p. 227

[17] Williams C.E., May R.P., Guinier A., in: *X-ray characterisation of materials*, Editor: E. Lifshin (Wiley-VCH, Weinheim, 1999)

[18] Bellmann D., Staron P., Becker P., Physica B **276-278**, 124 (2000)

[19] Agamalian M., Christen D K., Drews A R., Glinka C.J., Matsuoka H., Wignall G.D., J. Appl. Cryst. **31**, 235 (1998)

[20] Sears, V.F., *Neutron scattering lengths and cross sections*, Neutron News **3**, 26 (1992)

[21] Goldberger, M. L., Seitz, F., Phys. Rev. **71**, 294 (1947)

[22] Sears, V.F., *Neutron Optics – An Introduction to the Theory of Neutron Optical Phenomena and Their Applications* (Oxford University Press, Oxford, 1989), p. 176

[23] Staron P., Bellmann D., J. Appl. Cryst. (submitted, 2000)

Figure Captions

Figure 1. Temperature of foaming Zn + ZrH_2. The inset shows a magnification of the melting range. The thermocouple is contacted with the precursor material which was placed on a pre-heated substrate. Time zero is 3 s later, when the furnace door is closed. Short vertical lines mark the times at which samples were removed to conserve different foaming stages. The open symbol denotes the point at which the sample softens (determined within a certain limit of accuracy). T_s(Zn), the literature value for the melting point of Zn, and the experienced melting temperature in the experiment are marked by dotted horizontal lines.

Figure 2. Experimental set-up for ultra small-angle neutron scattering (USANS) measurements using a double crystal diffractometer (DCD).

Figure 3. Some measured (symbols) and calculated (lines) USANS curves of unfoamed and foamed zinc samples. The rocking curve (spectrometer function) without sample is also displayed.

Figure 4. Differential macroscopic cross section for unfoamed and foamed zinc samples.

Figure 5. Optical micrographs of zinc samples: left: unfoamed, right: foamed for 120 s. Width of field is 1.2 mm in both cases.

Figure 6. SEM images of foamed Zn samples. (a) sample without blowing agent, (b) sample with blowing agent (unfoamed), (c) and (d) foamed for 110 s, (e) foamed for 120 s. Inset of (b) shows a region of the sample magnified 3 times.

Figure 7. Upper: particle size distribution of loose ZrH_2 powder determined by laser particle analysis. Lower: size distribution *v(D)* of scattering centres in pressed zinc powder samples with and without zirconium hydride measured by USANS.

Figure 8. Length change of foamable Zn+0.3wt.% ZrH_2 material heated in a sintering dilatometer (argon atmosphere, measuring force 2.5 N). Results for three different heating conditions are given.

Figure 9. Pore size distributions *v(D)* in zinc foams. Upper: entire size range with inset showing volume fraction for 0.5, 1 and 5 μm size of scattering centres as a function of time, lower: semi-logarithmic representation restricted to scattering centres with small volume fractions.

Figure 10. Total volume fraction V'_{tot} of pores in foamed zinc as a function of foaming time at 440 °C determined by buoyancy measurement and USANS. The dotted lines are merely for orientation, whereas the dashed line represents a linear fit $V'_{tot}=0.102 + 0.0079$ t.

Tables

Table 1. Methods for investigating metal foams grouped according to whether two-dimensional projections or true three-dimensional images are obtained, whether early (pore diameters ≤ 1 μm) or late (pore diameters ≥ 1 μm) evolution states of a foam are invoked and whether pre-manufactured foams are investigated ex-situ or expanding foams are looked at in-situ. Methods used in this paper have been underlayed in grey.

	2D		**3D**	
	foaming stage			
	early	**late**	**early**	**late**
in-situ	-	-	X-ray microradioscopy	X-ray radioscopy neutron radioscopy ultrasound monitoring **dilatometry**
ex-situ	**electron microscopy**	**optical microscopy** image analysis	X-ray microtomography SANS **USANS**	X-ray tomography

Table 2. Unfoamed and foamed zinc samples used for the USANS measurements. Relative densities are based on a weighted average of the density for bulk Zn: (7.133 g/cm^3) and ZrH_2 (5.47 g/cm^3). The experimental accuracy for density measurements is ± 0.02 g cm^{-3}, for the porosity ± 0.3%.

composition of sample	**foaming time t (s)**	**density (g cm^{-3})**	**porosity (%)**
Zn	0	7.06	0.9
Zn + 0.3 wt.% ZrH_2	0	7.05	1.1
Zn + 0.3 wt.% ZrH_2	60	7.06	1.0
	70	7.04	1.2
	80	6.98	2.1
	90	6.99	1.9
	100	6.99	1.9
	110	6.94	2.6
	115	6.43	9.8
	120	5.82	18.4

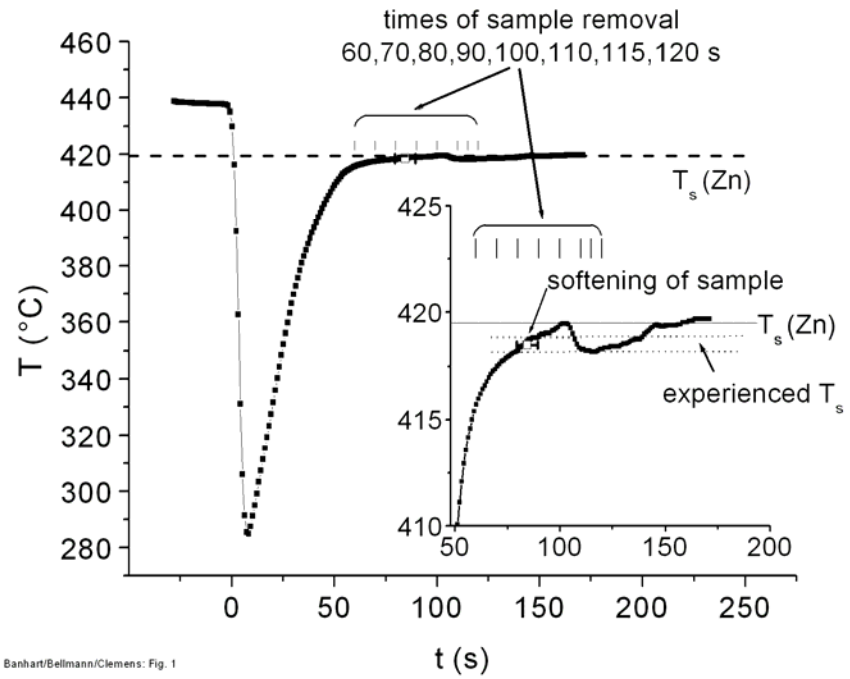

Figure 4. Temperature of foaming Zn + ZrH_2. The inset shows a magnification of the melting range. The thermocouple is contacted with the precursor material which was placed on a pre-heated substrate. Time zero is 3 s later, when the furnace door is closed. Short vertical lines mark the times at which samples were removed to conserve different foaming stages. The open symbol denotes the point at which the sample softens (determined within a certain limit of accuracy). T_s(Zn), the literature value for the melting point of Zn, and the experienced melting temperature in the experiment are marked by dotted horizontal lines.

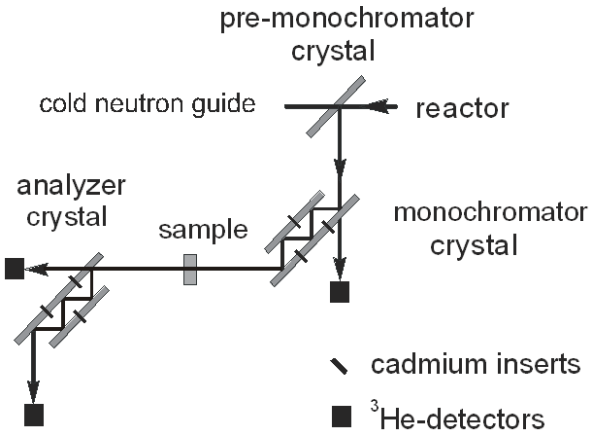

Figure 5. Experimental set-up for ultra small-angle neutron scattering (USANS) measurements using a double crystal diffractometer (DCD).

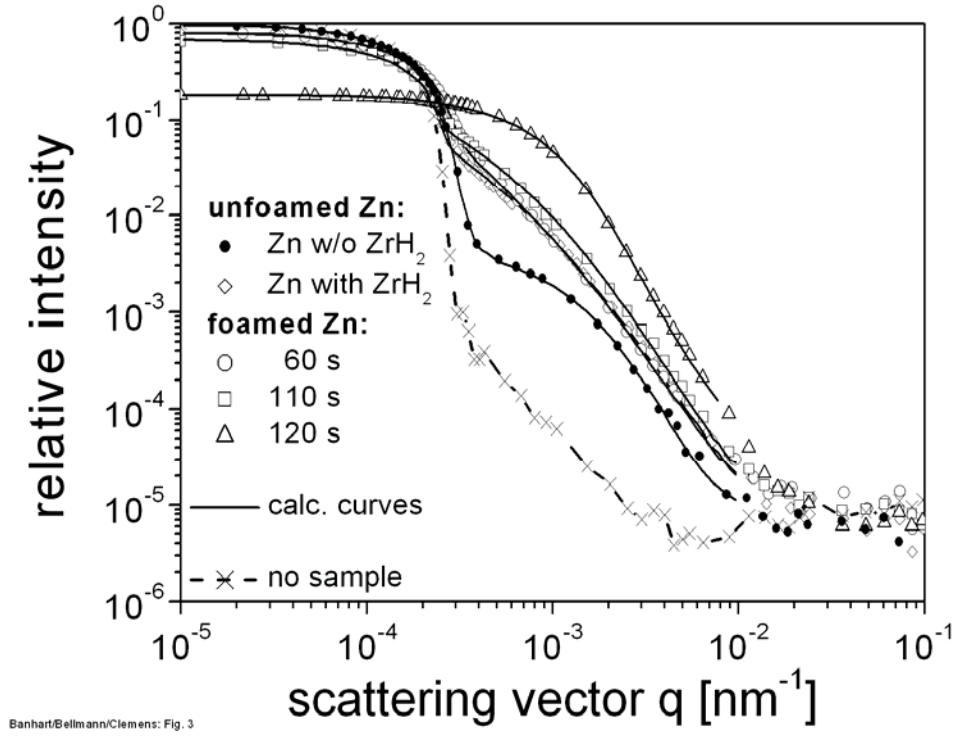

Figure 6. Some measured (symbols) and calculated (lines) USANS curves of unfoamed and foamed zinc samples. The rocking curve (spectrometer function) without sample is also displayed.

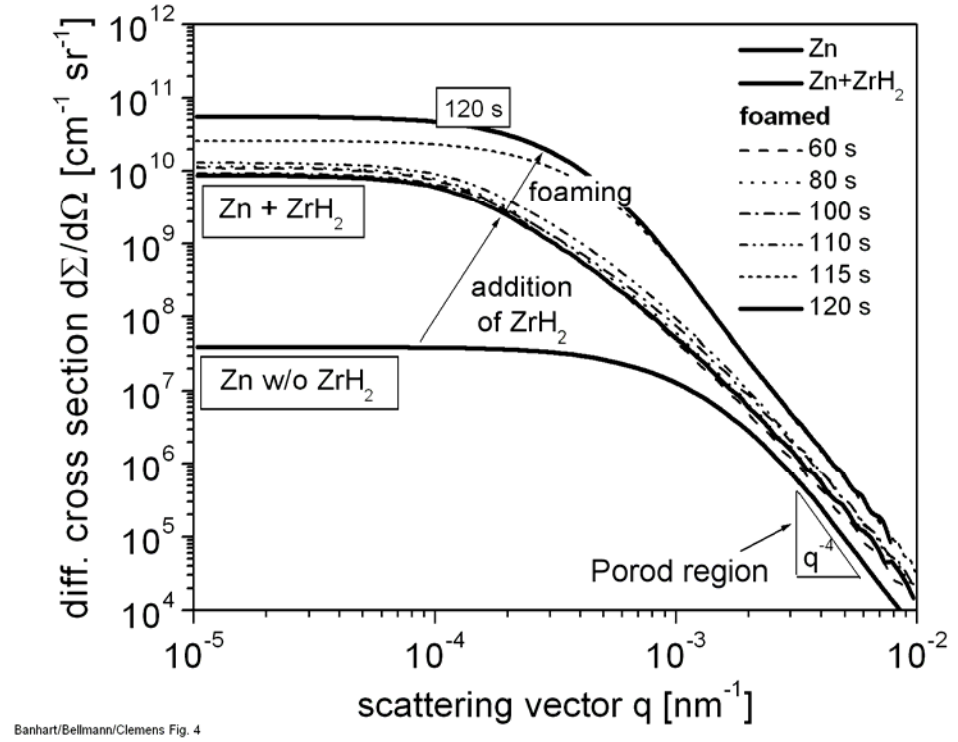

Figure 4. Differential macroscopic cross section for unfoamed and foamed zinc samples.

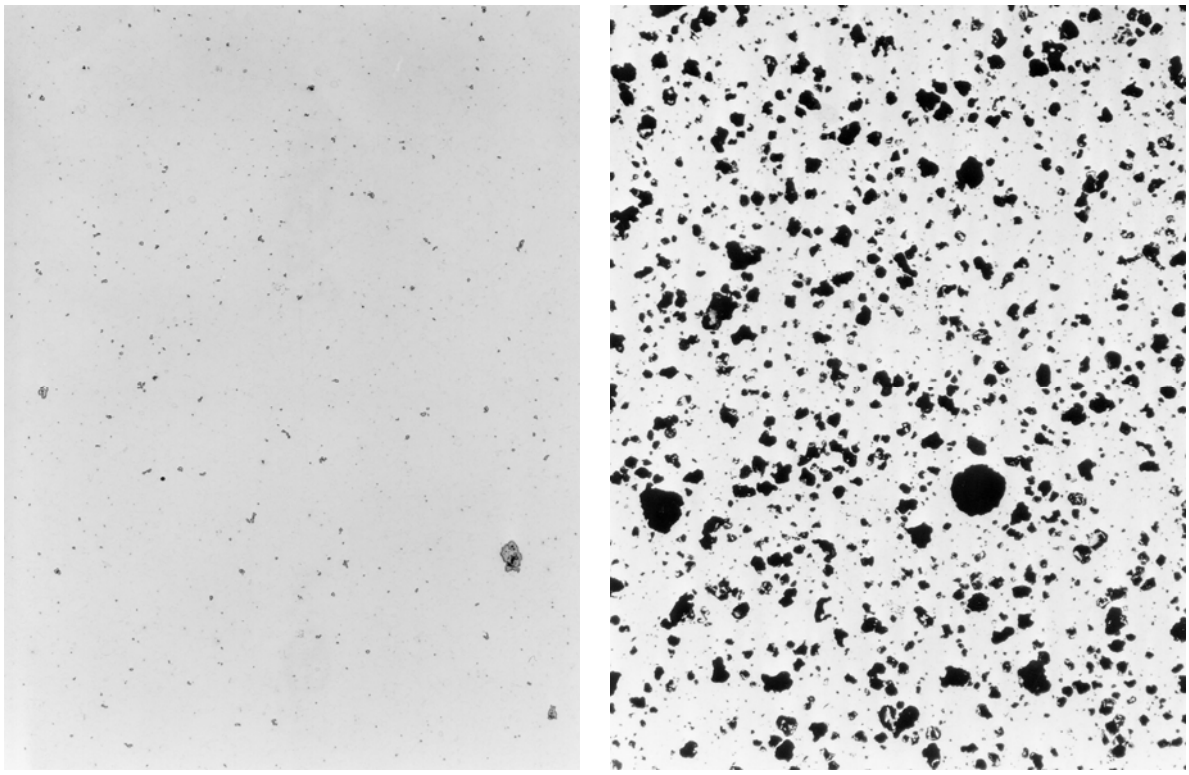

Figure 5. Optical micrographs of zinc samples: left: unfoamed, right: foamed for 120 s. Width of field is 1.2 mm in both cases.

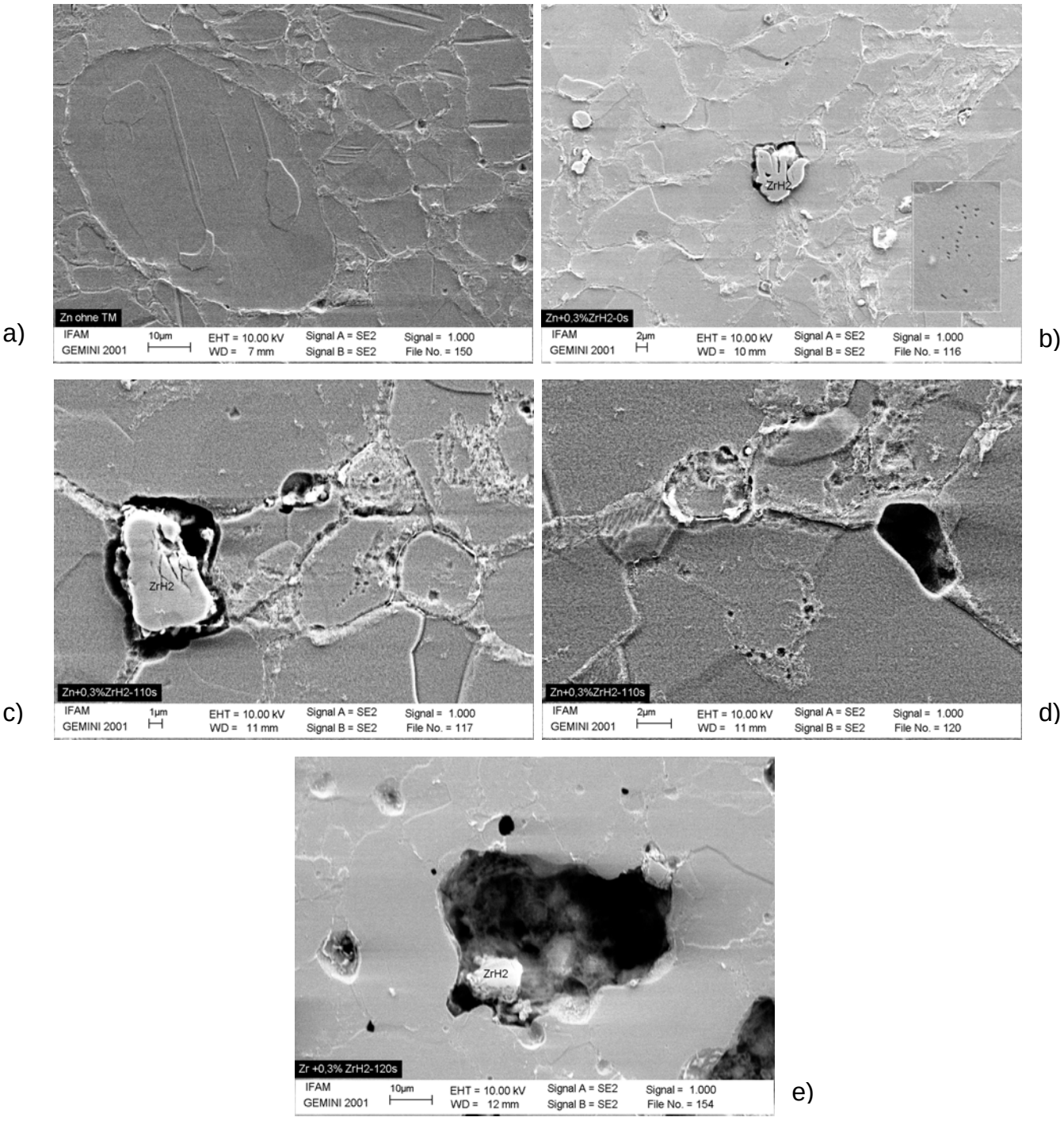

Figure 6. SEM images of foamed Zn samples. (a) sample without blowing agent, (b) sample with blowing agent (unfoamed), (c) and (d) foamed for 110 s, (e) foamed for 120 s. Inset of (b) shows a region of the sample magnified 3 times.

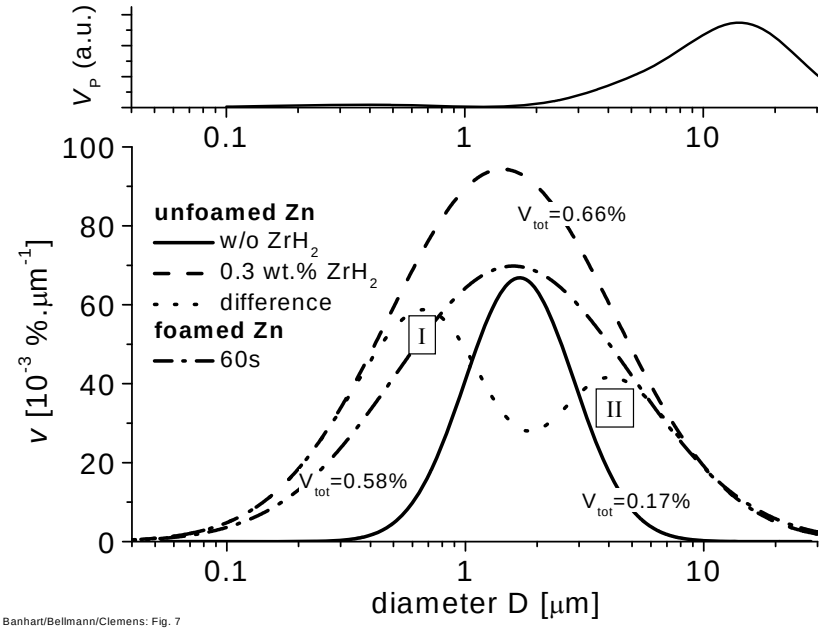

Figure 7. Upper: particle size distribution of loose ZrH_2 powder determined by laser particle analysis. Lower: size distribution *v(D)* of scattering centres in pressed zinc powder samples with and without zirconium hydride measured by USANS.

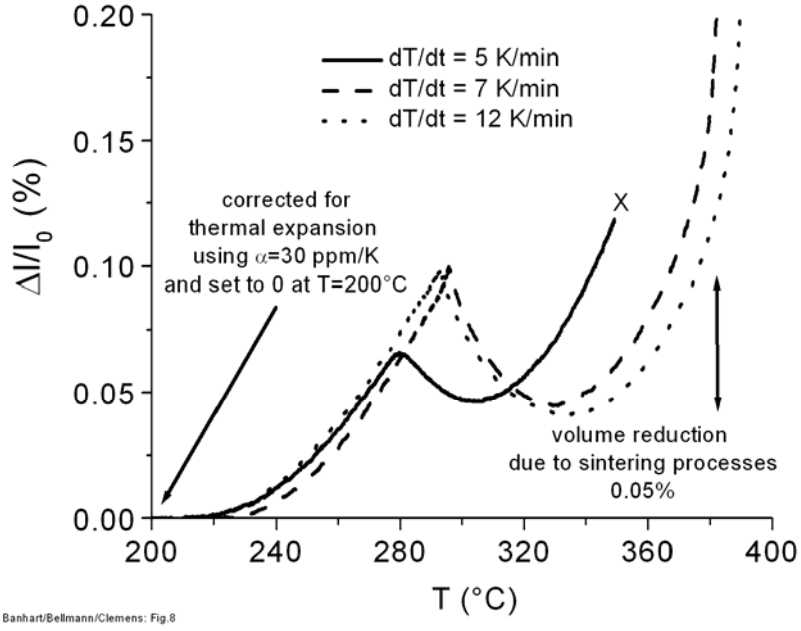

Figure 8. Length change of foamable Zn+0.3wt.% ZrH_2 material heated in a sintering dilatometer (argon atmosphere, measuring force 2.5 N). Results for three different heating conditions are given.

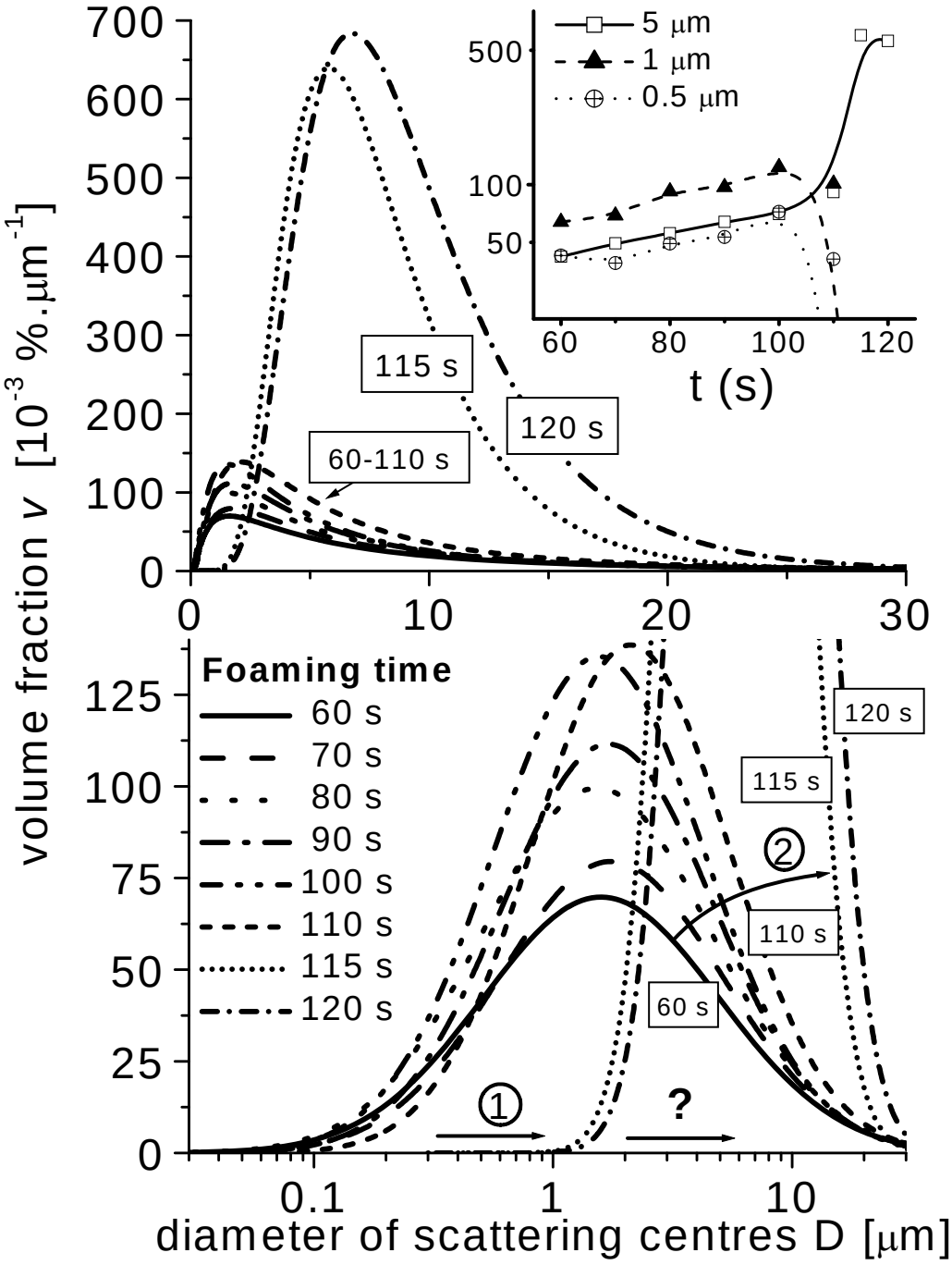

Banhart/Bellmann/Clemens: Fig. 9

Figure 9. Pore size distributions *v(D)* in zinc foams. Upper: entire size range with inset showing volume fraction for 0.5, 1 and 5 μm size of scattering centres as a function of time, lower: semi-logarithmic representation restricted to scattering centres with small volume fractions.

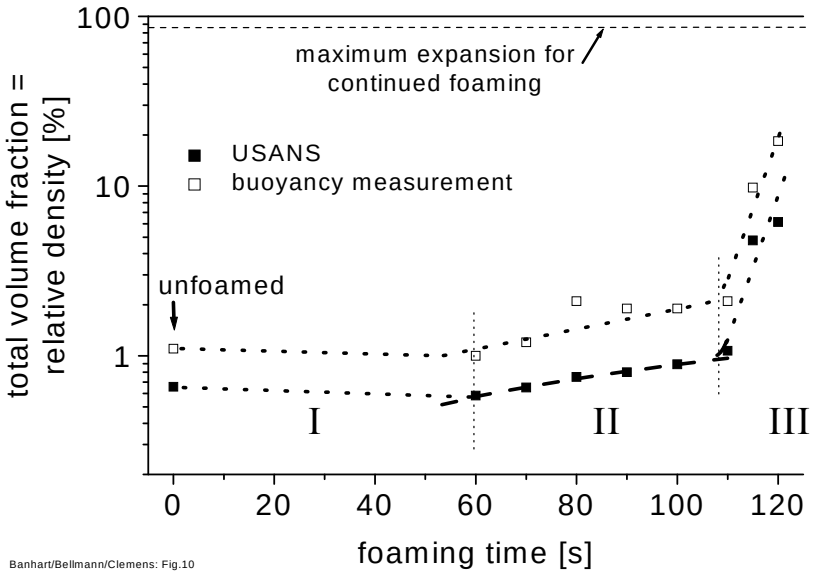

Figure 10. Total volume fraction V'_{tot} of pores in foamed zinc as a function of foaming time at 440 °C determined by buoyancy measurement and USANS. The dotted lines are merely for orientation, whereas the dashed line represents a linear fit $V'_{tot}=0.102 + 0.0079$ t.